

Small-Angle X-ray Scattering Demonstrates Similar Nanostructure in Cortical Bone from Young Adult Animals of Different Species

Jørn Døvling Kaspersen¹ · Mikael Juhani Turunen^{1,2} · Neashan Mathavan¹ · Sebastian Lages³ · Jan Skov Pedersen⁴ · Ulf Olsson⁵ · Hanna Isaksson¹

Received: 10 November 2015 / Accepted: 15 February 2016 / Published online: 25 February 2016
© Springer Science+Business Media New York 2016

Abstract Despite the vast amount of studies focusing on bone nanostructure that have been performed for several decades, doubts regarding the detailed structure of the constituting hydroxyapatite crystal still exist. Different experimental techniques report somewhat different sizes and locations, possibly due to different requirements for the sample preparation. In this study, small- and wide-angle X-ray scattering is used to investigate the nanostructure of femur samples from young adult ovine, bovine, porcine, and murine cortical bone, including three different orthogonal directions relative to the long axis of the bone. The radially averaged scattering from all samples reveals a remarkable similarity in the entire q range, which indicates that the nanostructure is essentially the same in all species. Small differences in the data from different directions confirm that the crystals are elongated in the [001] direction and that this direction is parallel to the long axis of the bone. A model consisting of thin plates is successfully employed to describe the scattering and extract the plate thicknesses, which are found to be in the range of 20–40 Å for most samples but 40–60 Å for the cow samples. It is demonstrated that the mineral plates have a large degree of

polydispersity in plate thickness. Additionally, and equally importantly, the scattering data and the model are critically evaluated in terms of model uncertainties and overall information content.

Keywords Bone · Nanostructure · Small-angle X-ray scattering · Wide-angle X-ray scattering · Mineral thickness

Introduction

Bone is a complex material with a hierarchical structure, where the main building blocks are the protein type I collagen and a crystalline mineral phase usually referred to as carbonated hydroxyapatite. These two very different components are closely associated in fibrils that form an interconnected network, with specific structural arrangement depending on species and type of tissue [1]. With collagen being tough but soft and hydroxyapatite being rigid but brittle, together they form a nanocomposite that provides bone with its unique mechanical properties of strength and toughness [2, 3].

The organization of collagen molecules within the fibrils is generally acknowledged to have a quarter-staggered array as originally proposed by Hodge and Petruska [4]. Collagen seems to act as a template for mineralization [5], but the exact association of the hydroxyapatite crystals with the collagen is still debated. The mineral structures have been indicated to be regularly organized thin plates within the collagen fibrils [6], however, mineralization also occurs on the fibril surface [7]. Possibly, the degree of intra- and extrafibrillar mineralization depends on the specific type of fibril array pattern [1]. Studies of deproteinated bone samples indicate that the mineral structures

✉ Hanna Isaksson
hanna.isaksson@bme.lth.se

¹ Department of Biomedical Engineering, Lund University, 221 00 Lund, Sweden

² Department of Applied Physics, University of Eastern Finland, 70 211 Kuopio, Finland

³ Max IV Laboratory, Lund University, 221 00 Lund, Sweden

⁴ Interdisciplinary Nanoscience Center and Department of Chemistry, Aarhus University, Aarhus, Denmark

⁵ Division of Physical Chemistry, Lund University, Box 124, 221 00 Lund, Sweden

still form a continuous phase [8, 9] or larger aggregates [10] even after the organic material has been removed, which disagrees with the classical view as the mineral structures existing as individual plates. This observation, however, agrees well with a recent structure revealed by transmission electron microscopy (TEM) of ion-milled thin sections, suggesting that most of the mineral structures are around the fibrils and are situated very tightly together [11–13]. The plate-like morphology has been proposed to be caused by preferred adsorption of either protein (see e.g., [14, 15]) or citrate [16] in the [100] direction of hydroxyapatite crystals, thereby causing growth inhibition in this direction.

X-ray diffraction (XRD) of bone suggests that the average hydroxyapatite crystals are 30–40 nm long and ~20 nm wide [17], containing significant imperfections [18, 19]. Still, the periodic lattice can be visualized by TEM [20]. The mineral structures have their crystallographic *c*-axis aligned almost parallel to the fibril axis (to our knowledge originally reported by Schmidt [21]), which is used to study the orientation of fibrils with e.g., XRD [22]. The length of the crystals in the *c*-axis direction has been shown to increase during developmental growth of the bone [17, 23] and reaches a constant value afterwards [24]. In addition to the crystal lattice, the hydroxyapatite nanocrystals have been shown to contain a significant layer of disordered and hydrated amorphous calcium phosphate-like material on the surface [25] as well as ordered water molecules [26, 27]. This surface layer may contribute to the apparent underestimation of the average crystal size as determined by XRD when compared to that obtained from TEM (discussed briefly in [28]). Also, TEM measures a small number of crystal sizes compared to XRD, which could explain the discrepancy in some cases due to size heterogeneity. A relatively large heterogeneity in the mineral sizes has been suggested to be important for bone strength [29].

Despite several decades of research, uncertainties regarding details of bone nanostructure still exist, mainly because bone nanostructure characterization *in vivo* is not possible. The complicated structure of bone warrants no single characterization technique substantially superior to the others, and therefore many different techniques have been used and are required to understand bone ultrastructure. The different techniques require different preparation steps for the bone tissue and probe the bone tissue at different levels or features, which may lead to slightly different results.

In this study, we use small-angle X-ray scattering (SAXS) at two experimental settings (extending into the wide-angle (WAXS) regime) to study the nanostructure of freshly cut cortical bone obtained in three different orthogonal directions relative to the bone long axis (see

inset in Fig. 1), as well as from animals of different species. When comparing bone nanostructure from different species it is desirable to obtain information on a large ensemble of crystals. In this respect, scattering techniques have an advantage over direct imaging techniques, e.g., TEM, which give information on fewer crystals. SAXS studies comparing different animals were conducted three decades ago [30, 31]. The instrumentation, however, has been significantly improved since these studies were conducted and therefore provides more detailed data. Assuming a known volume fraction and using only the high-*q* region of the data, Fratzl et al. developed a method to obtain a thickness parameter [32] which is now regularly used in studies of bone structure [33]. However, more elaborate models have been developed [34, 35], where a larger *q* range is used in the data analysis. Combinations of SAXS and WAXS can now also be used to obtain both the fibril directions and average crystal sizes, respectively [36], and the 3D predominant fibril orientation in bone is even being obtained using 3D scanning SAXS [37]. Two-dimensional fitting of statistical models are also being developed [38].

Despite recent progress in the field, there is still a need for better understanding of the scattering data and the accuracy and reliability of the results when different models are employed. The complex structure of bone and the high mineral volume fraction causes the scattering signal to be influenced by both the crystal shape and the

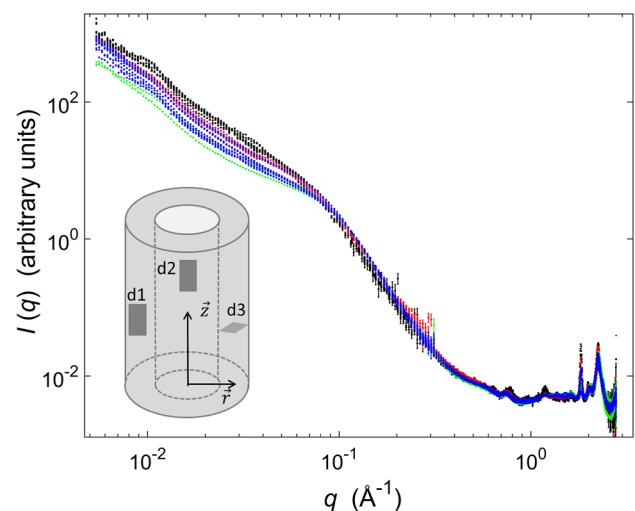


Fig. 1 Plot of the integrated intensity from the scattering curves from all bone samples: bovine (black), ovine (blue), porcine (red), and murine samples (green). The intensity has been scaled and an adjustable, constant background has been subtracted. The inserted drawing demonstrates the three different anatomically orthogonal directions of bone, where the direction is defined as normal to the slice. *d1* is perpendicular to both \vec{z} (the long axis of the bone) and \vec{r} , *d2* is perpendicular to \vec{z} and parallel to \vec{r} , and *d3* is parallel to \vec{z} and perpendicular to \vec{r} (Color figure online)

correlation between neighboring crystals. Here, we present SAXS and WAXS data from different species and demonstrate the similarity of bone structure on a wide length scale. We use a previously developed model [34] to describe the data, followed by a thorough evaluation of the model and a discussion of the information it provides as well as the uncertainty of the model parameters.

Materials and Methods

Sample Overview

Freshly cut cortical bone samples from the mid-diaphysis of the femur of several different animals were used in this study. Moreover, bone samples were obtained in different anatomically orthogonal directions. The directions named d1, d2, and d3 are obtained perpendicular to each other (Fig. 1). The samples include ovine (d1, d2, and d3), porcine (d2 and d3), bovine (d2 and d3), and murine (d3) cortical bone. The ovine and porcine animals were around 8 months old, and the bovine animal was around 20 months old. These were all obtained from the local abattoir. Therefore, their exact age is not known. The murine animal was 10 weeks old (Sprague–Dawley rat, Approved by the local Ethical committee, M64-13). Hence, all animals had passed sexual maturity but were possibly still growing. Thus, they were all in the range of adolescent to adults.

Sample Preparation

Sectioning was achieved using a diamond blade saw system under constant water irrigation (EXAKT 300 CP Diamond Band Saw, Norderstedt, Germany) to obtain samples of approximately 0.5–0.75 mm thickness. Samples were subsequently wrapped in phosphate buffered saline (PBS) soaked gauze and stored at $-20\text{ }^{\circ}\text{C}$ until measurements.

Measurements and Initial Data Reduction

All measurements were performed on the Ganesha 300XL from JJ X-Ray Systems Ap at Department of Physical Chemistry, Lund University, at a wavelength of $1.54\text{ }\text{\AA}$. Acquisition times for high and low q , respectively, were 3600 and 7200 s for the bovine samples and 1800 and 3600 s for all other samples. The samples were mounted on the holder using tape, and the holder was inserted into the vacuum chamber. Hence, the bone samples were not hydrated during measurements, but were kept in saline solution before and after. Two to three different spots (spot size 2 mm in diameter) were measured on each bone

sample, and for each spot two q ranges were measured: a low- q region around $0.006\text{--}0.3\text{ }\text{\AA}^{-1}$ and a high- q region around $0.1\text{--}2.8\text{ }\text{\AA}^{-1}$. Dark current subtraction and azimuthal integration was performed using the Saxsgui program (Saxsgui v2.13.02, Rigaku Innovative Technologies, Inc., and JJ X-ray Systems Aps), and the integrated data were scaled in the overlapping q region to assure physically sensible data using routines written in Matlab (Matlab 2015a, The MathWorks, Inc., Natick, MA, USA).

SAXS Data Analysis and Modeling

The model developed by Bungler et al. [34] was used in this study. Briefly, this method assumes that the mineral crystal, due to its higher electron density than collagen, dominates the scattering, and that the mineral structures have the shape of a plate that is infinite (or larger than the distance probed with the measurements) in two dimensions and a thickness of T in the third dimension. The form factor of such an infinite plate is

$$P(q) = \frac{1}{q^2} \left(\frac{\sin(qT/2)}{qT/2} \right)^2. \quad (1)$$

Note that this form factor corresponds to randomly orientated particles with a homogeneous electron density, which may not necessarily be a good approximation at the length scale of the thickness, T . As will be discussed later, the plates do not all have the same thickness, so it is necessary to include thickness polydispersity to describe the data. Using the Schulz–Zimm distribution [39], $D(T, T_{\text{av}})$, where T_{av} is the average plate thickness, the scattering can be calculated analytically for rapid assessment of the average form factor:

$$P_{\text{av}}(q) = \frac{\int_0^{\infty} T^2 P(q) D(T, T_{\text{av}}) dT}{\int_0^{\infty} T^2 D(T, T_{\text{av}}) dT}. \quad (2)$$

However, as the volume fraction of mineral structures in bone is high, neighboring crystals will be closer together in space and thereby influence the possible positions and orientation they can obtain. These excluded volume effects have been taken into account with the random phase approximation (RPA) as proved to work for stiff polymers [40]:

$$P_{\text{eff}}(q) = \frac{P_{\text{av}}(q)}{1 + \nu P_{\text{av}}(q)}, \quad (3)$$

where ν is a parameter describing the interaction strength and which increases with increasing concentration. Simulations have shown that the random phase approximation, though to our knowledge not proved theoretically to work for thin plates, is indeed able to describe the scattering from a system of plate-like particles (CLP Oliveira and JS

Pedersen, unpublished). Finally, the observed increase in intensity at low q is explained by variations in the electron density at longer length scales due to inhomogeneity in the size and distribution of the crystals. These variations can be described as a fractal system, so an effective fractal structure factor [41] is included in the final expression:

$$I(q) = P_{\text{eff}}(q)(1 + A_{\text{fractal}}q^{-\alpha}). \quad (4)$$

Here α is the fractal dimension and A is a parameter scaling the contribution. Note that the fractal structure factor is merely included to fit the low- q region of the scattering and is not used to derive physical quantities. The adjustable parameters in the fitting (performed with home-written software) are thereby the thickness (T), the relative standard deviation of the thickness distribution ($\sigma_{\text{poly,rel}}$), an overall scale factor, the parameter from RPA (ν), the two parameters from the fractal structure factor (A_{fractal} and α), and a constant background. Since the fractal power law and the background describe the low- and high- q region, respectively, the effective q range for determining the information content in our data will be about $0.03\text{--}0.6 \text{ \AA}^{-1}$. If the maximum particle dimension, D_{max} , is taken as q_{min}/π , the upper limit for the number of independent parameters that can be determined from the data is ~ 20 . Therefore, we have enough information to fit the remaining four parameters (scale, RPA value, thickness, and polydispersity) for this q range. The practical aspects of the fitting will be discussed in the following.

Results

Strikingly Similar Scattering Curves from Different Animals

All measured scattering curves from the fresh bone samples are displayed in Fig. 1. For comparison, the curves were scaled to each other and an adjustable constant background was applied using a weighted least-squares procedure in Matlab. It is immediately observed that the scattering from the different species and directions is remarkably similar. This similarity over the entire q range indicates that the nanostructure of the different bone samples is highly comparable in terms of plate thickness (intermediate q), atomic crystal structure (high q), and to a large degree also the inter-particle separations (low q). We note that the absence of a visible correlation peak for the inter-particle distances directly reveals that mineral plates do not possess long-range translational order, i.e., they are not arranged in a well-organized “deck of cards” structure as initially believed [28] and still occasionally depicted in more recent publications [1].

Anisotropic Scattering Data Confirms Bone Directionality

Representative 2D scattering datasets from ovine bone for the three different bone directions (defined in Fig. 1) are shown in Fig. 2 for both low- q (Fig. 2a–c) and high- q (Fig. 2d–f) data. All our low- q datasets contain some degree of anisotropy, which is in general larger in direction d1 and d2 compared to that of d3, and more or less parallel to the long axis of the bone. The high- q data provide information on both the anisotropy and the preferred orientation of the mineral crystals. The innermost visible Bragg peak arises from the crystallographic (002) plane, which is the longest dimension of the hydroxyapatite crystals in bone [17]. In the d1 and d2 samples, the (002) peak forms an arc, which proves that the c -axis has a preferred orientation. The radial directions with the largest intensity in the (002) arc in d1 and d2 at high q (Fig. 2d, e) correspond to the directions at low q (Fig. 2a, b) where the intensity falls off most abruptly, i.e., the direction with the largest dimension. Our data thereby confirm that the [001] crystallographic direction (the c -axis) has the longest dimension. From Bragg’s law and the crystal spacing, it is found that first-order diffraction from the (002) plane is observed when the angle between the c -axis and the beam is around 77° . This (002) peak is barely visible in the d3 sample, thereby revealing that the c -axis is mostly parallel to the long axis of the bone. The small intensity of the (002) peak from d3 relative to d1 and d2 is also clearly shown in Fig. 3, which shows the Bragg region of the radially averaged scattering data.

Good Model Fits and Sensible Fit Results for All Datasets

The model fits to all datasets are presented in Fig. 4 (the data were fit to 1 \AA^{-1} as the model does not include atomic resolution) and the parameters from the optimization in Fig. 5. The model can provide visually very good fits to all datasets, and the somewhat large χ^2 values (smaller value means better fit quality) are partly caused by very small error bars on the data. Additionally, some features are not included in the model, like the small collagen peak at around 0.01 \AA^{-1} , which therefore result in larger χ^2 values. For the ovine, porcine, and murine samples, the most interesting parameter, the thickness (T), is around $20\text{--}40 \text{ \AA}$, while for the bovine samples it seems to be consistently larger at around $40\text{--}60 \text{ \AA}$. The other parameters (except the relative polydispersity) are also somewhat different for the bovine samples compared to the rest, with higher ν (from RPA) and scale factor for the fractal structure factor (A_{fractal}), but lower value of the fractal dimension (α)

Fig. 2 Demonstration of anisotropy in the scattering data from ovine bone. The low- q data in direction d1 (a), d2 (b), and d3 (c), and the corresponding high- q data from d1 (d), d2 (e), and d3 (f)

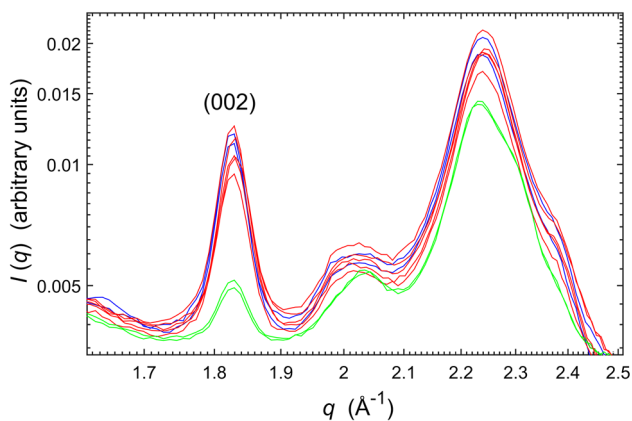
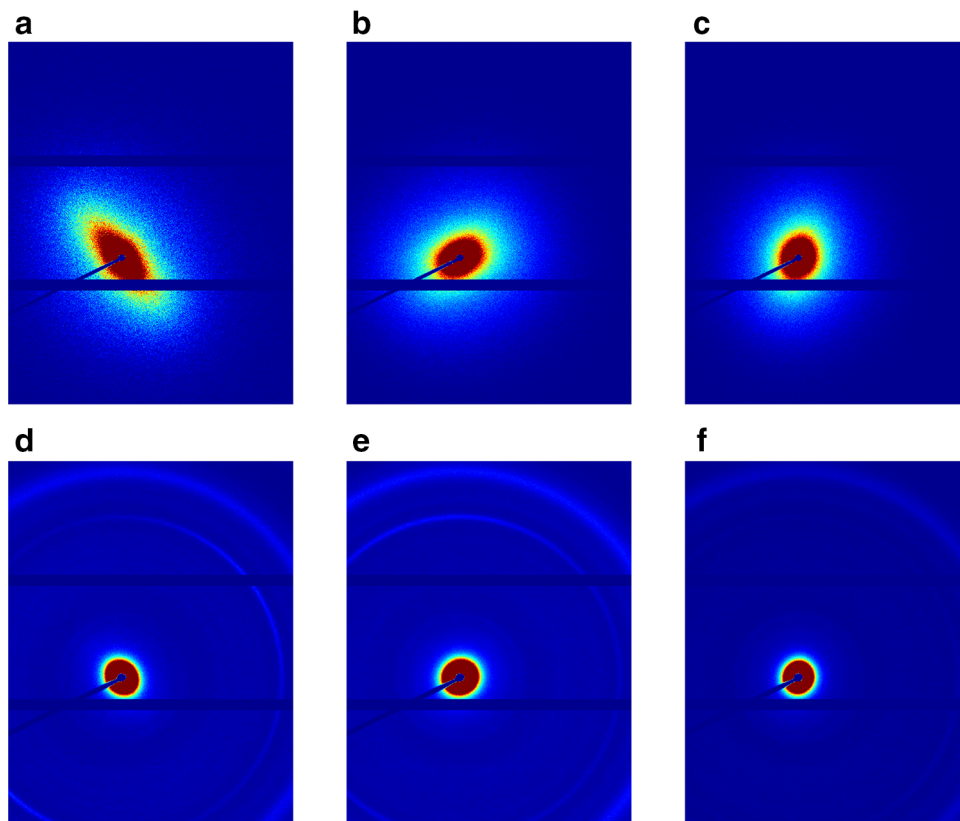


Fig. 3 Azimuthally integrated average of a region of the high- q data for all ovine samples demonstrating the small (002) peak of the d3 bone direction (green) relative to d1 (blue) and d2 (red) (Color figure online)

(Fig. 5). Moreover, the bovine samples generally show higher uncertainties in the fitted parameters.

To assure that the different values for T are not caused by different local minima with similar fit quality in the solution space, we additionally performed a fit to the data with fixed values of both ν (0.02), α (2.3), and relative polydispersity (0.4). These values were based on the results

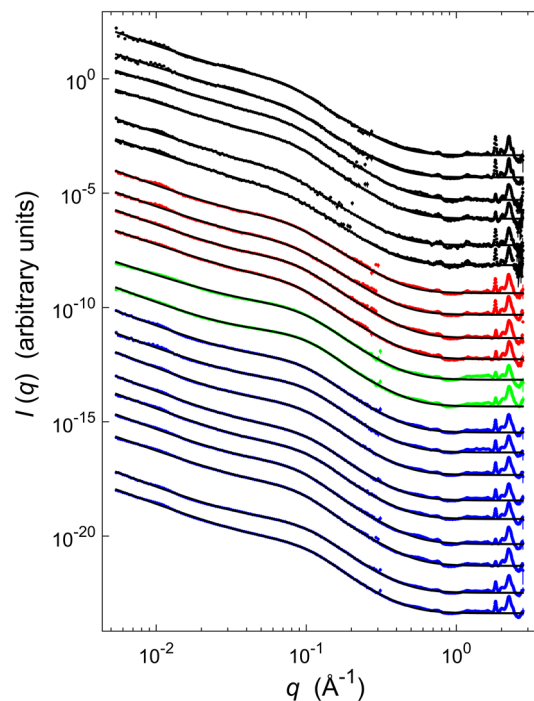


Fig. 4 Fit quality of the best fits to all datasets. The color coding is bovine (black), ovine (blue), porcine (red), and murine (green) bone (Color figure online)

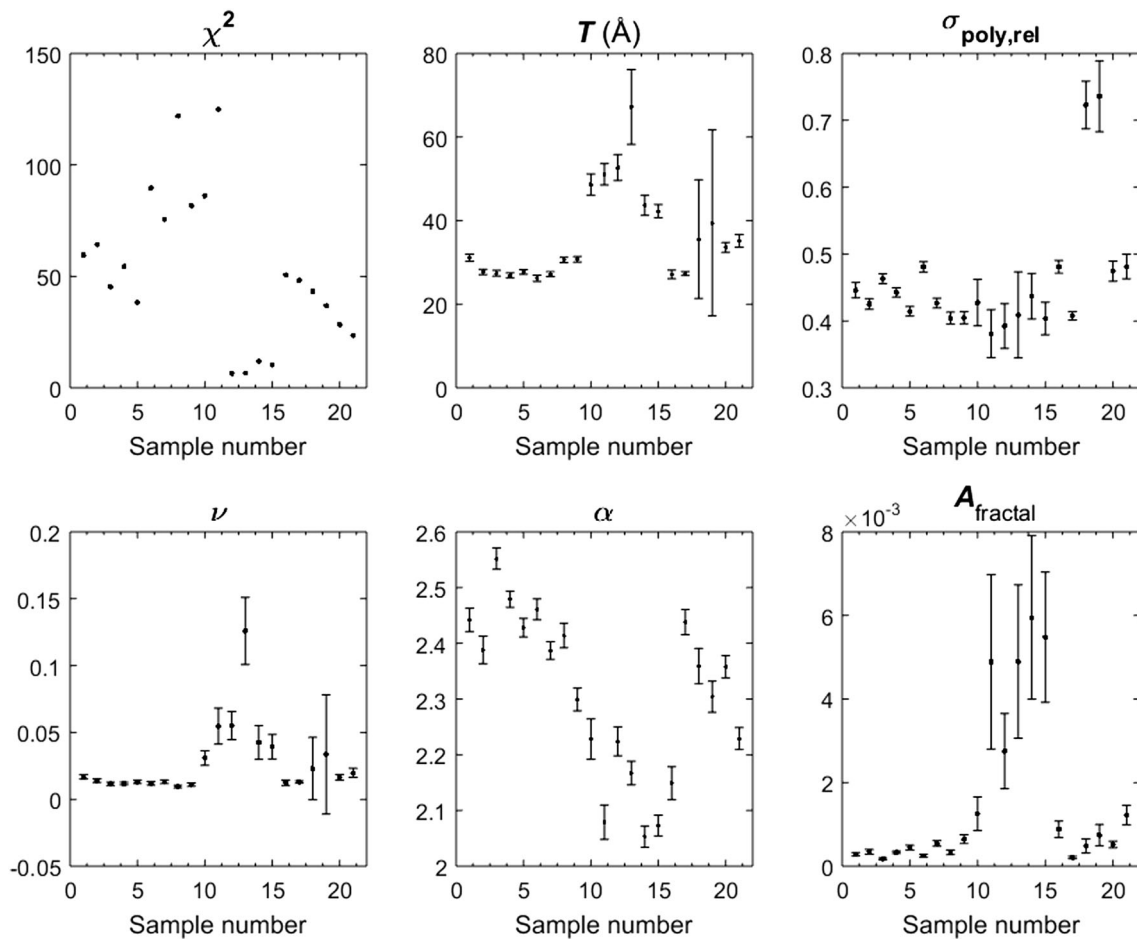


Fig. 5 Resulting parameters from the fits shown in Fig. 4: fit quality (χ^2), thickness (T), relative polydispersity ($\sigma_{\text{poly,rel}}$), the parameter from RPA (ν), and the two parameters describing the low- q region (α and A_{fractal}). The numbering of the samples on the x -axis: Ovine d1

(1–2), ovine d2 (3–7), ovine d3 (8–9), bovine d2 (10–13), bovine d3 (14–15), murine d3 (16–17), porcine d2 (18–19), and porcine d3 (20–21)

of the fit with all parameters optimized, and the fit allows for a better relative comparison of the thickness. Even with these parameters fixed, the fit quality is almost the same (results not shown), and both the large error bars on the d2 sample from the porcine samples and the large difference in scale factor of the fractal aggregates disappear. However, most importantly, the trend with thicker plates for the bovine samples persists. This test therefore supports the initial indication from our data, namely that the bovine samples apparently have thicker mineral plates compared to the other species.

Large Deviation from Simple Plate form Factor Reveals Polydispersity

A plot of a simple plate form factor ($T = 30 \text{ \AA}$) with a representative dataset is shown in Fig. 6a (black line and red dots, respectively) together with a line with q^{-4} dependency (blue line). It is obvious that the simple plate form factor is far off from the measured data. At the low-

q region, the measured data deviate from the q^{-2} dependency of a plate form factor, which can be explained by structure factor effects due to the high volume fraction of mineral crystal in the bone. The thickness has not been optimized for the best fit in this plot, but a change in thickness will only move the subsidiary minima and maxima to higher or lower q . The only way to reach the observed q^{-4} dependency in the intermediate q range is to smear the form factor with a large polydispersity in T , which is thereby immediately observed from this figure.

Discussion

Complex Bone Structure Causes Complex Scattering Data

Since the bone nanostructure is known to be very complex, it is expected that the scattering data will be difficult to analyze. In that respect, it is remarkable how similar the

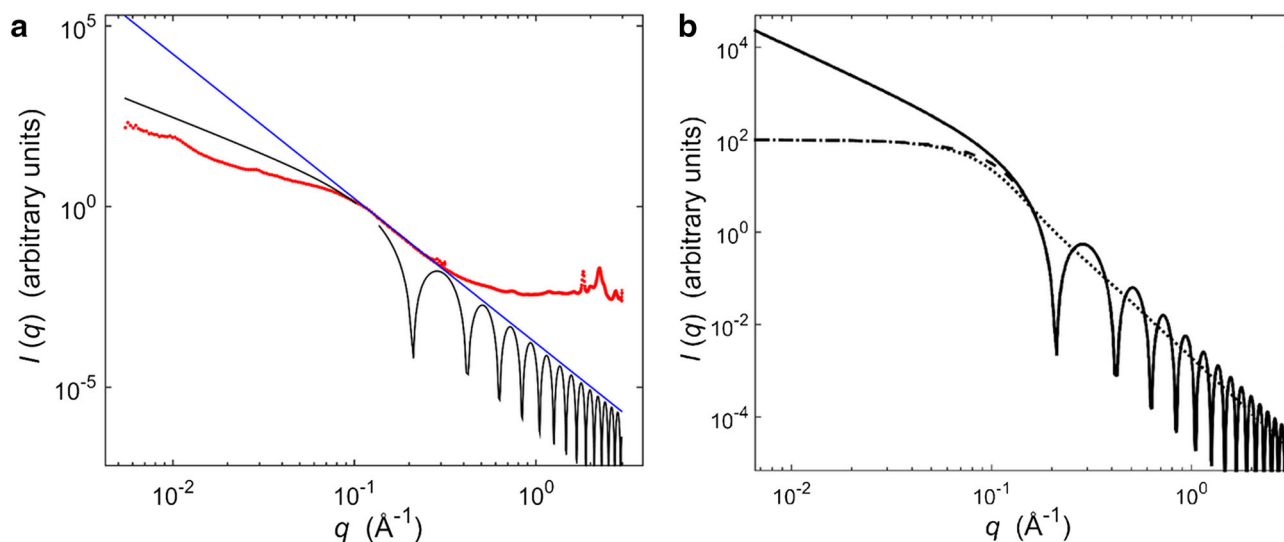


Fig. 6 **a** Plot of a representative dataset (*red points*), the form factor of a plate with a thickness of 30 Å (*black line*), and a slope of q^{-4} (*blue line*). **b** Plate form factor with thickness 30 Å (*solid line*), with

the influence of an RPA value of 0.01 (*dashed line*), and the additional effect of a relative polydispersity of 0.4 (*dotted line*) (Color figure online)

scattering data in Fig. 1 are. This observation demonstrates that, despite its complexity, the nanostructure of bone is very similar between different species. The observed differences at low q most likely result from small differences in thickness and degree of mineralization, which influence both the excluded volume effects and the fractal-like variations. As the samples were placed in vacuum during measurements, some degree of dehydration is unavoidable. However, as our focus lie mostly on the crystals thickness and only the outmost 10 % is expected to contain water [26], any thickness decrease due to water evaporation in the surface region is believed to be negligible at our resolution. Furthermore, since the aim of the study is to compare different species, any small change due to dehydration will be the same for all samples.

At the intermediate q values, all data follow a clear q^{-4} dependency caused by a large degree of polydispersity. If both intra- and extrafibrillar mineral structures exist, a potential difference in average size between these may explain some of the observed polydispersity. Also, a structure like the one shown in [13], where the extrafibrillar structures consist of different numbers of thin plates very close together, could resemble polydispersity in scattering experiments if the plates are tightly connected. Interestingly, our intermediate region with the observed q^{-4} dependency corresponds to the high- q region of most standard SAXS setups, which is used to extract the plate thickness with the method introduced by Fratzl et al. [32]. As a rule of thumb, the Porod law applies from the first subsidiary maximum in the form factor, which is quite far from the region in our data that actually shows a q^{-4} dependency. Therefore, it is possible that thicknesses extracted using the Porod constant are imprecise.

In the high- q region, the differences in the Bragg peaks are caused by directionality of the bone samples (Figs. 2d–f, 3). Similar degree of anisotropy in the d1 and d2 directions is expected if the plates are situated in concentric layers around osteons, which themselves are on average parallel to the long axis of the bone [42]. The observed desmearing of the anisotropies is probably caused by a disordered fibrillar phase [1] and a spiral twisting of the fiber orientation around the osteons [42], while the small degree of anisotropy in d3 is probably merely due to local directionality in the limited irradiated area.

From the fit results, it is noteworthy that the average thicknesses are rather similar (for example for the ovine samples) despite the large polydispersity. Due to this polydispersity, one would expect the average thickness to show a larger variation, however, the size distribution is apparently quite well determined from the fit procedure. Only the fitting results of the two measurements on the d2 porcine sample stand out by having larger relative polydispersities and larger error bars on T and α .

Correlation Between Plate Thickness and Polydispersity

In SAXS data, the Guinier region holds information about the radius of gyration, R_g , which is a model-independent measure of the average size of the particles in the sample. For large plates, there will be two Guinier regions, one from the maximum distances in the plane of the plate at very low q (which is not observed here due to structure factor effects or very large plates), and one from the thickness (T). The Guinier region for the thickness is the q

region up to where the data start to deviate significantly from a slope of q^{-2} , which for the shown plate form factors in Fig. 6a, b is around $q = 0.1 \text{ \AA}^{-1}$. However, when a polydispersity distribution of the thickness, $D(T, T_{\text{av}})$, is present, the so-called z -averaged radius of gyration from the thickness of an infinite disc can be calculated approximately as

$$R_{\text{g}}^2|_z = \frac{1}{12} \frac{\int_0^\infty T^4 D(T, T_{\text{av}}) dT}{\int_0^\infty T^2 D(T, T_{\text{av}}) dT}. \quad (5)$$

From this expression, it is evident that a change in the observed position of the Guinier region can to some extent be caused by either a change in thickness, in polydispersity, or in both, so one should be cautious when optimizing the two simultaneously.

Excluded Volume Effects also Influence the Thickness Determination

As described above, the thickness is mainly determined from the Guinier region in the data, where the slope starts to deviate from q^{-2} . Therefore, the excluded volume effects should preferably not influence this region, whereby the random phase approximation would not either. However, Fig. 6b demonstrates that the RPA, even for a rather low ν value of 0.01 (dashed line) significantly influences the Guinier region of a plate form factor of $T = 30 \text{ \AA}$ (solid line). Additionally, if a relative polydispersity of 0.4 is included (dotted line), almost none of the features of the original plate form factor are left. The model does of course take these effects into account; however, since the RPA is only an approximation, the presence of excluded volume effects into the Guinier region will affect the precision of the thickness determination. Using PRISM theory [43], one could attempt to modify the RPA further as

$$P_{\text{PRISM}}(q) = \frac{P_{\text{av}}(q)}{1 + \nu P_{\text{av}}(q)c(q)}, \quad (6)$$

where $c(q)$ is the Fourier transform of the direct correlation function between the plates. A suitable choice for $c(q)$ may cause the resulting structure factor to affect the Guinier region to a lesser extent, however, it is not obvious what a good choice of this function would be. As the positions of the plates are impacted by biological control, it is not possible to calculate their theoretical correlations without knowing the control mechanism in more detail. Note that the apparent correlation between large thickness and large value of ν for the bovine samples could also have a physical explanation: If the number density of plates is similar in the different animals, thicker plates would mean larger volume fraction and thereby an increase in the excluded volume effect.

Relatively Large Solution Space for the Thickness Parameter

To evaluate the solution space of the thickness, we have performed a series of fits (up to $q = 1 \text{ \AA}^{-1}$) keeping T fixed and all other parameters optimized. Figure 7a shows the fits where T varies from 20 to 200 \AA in steps of 10 \AA . Figure 7b–d shows χ^2 , the relative polydispersity, and the value of ν from the excluded volume effect as a function of different thicknesses in the range 15–120 \AA . It is obvious from Fig. 7a that the fits are very similar despite the large difference in plate thickness. From the χ^2 -values in Fig. 7b it can be seen that there seems to be an optimum around $T = 20\text{--}40 \text{ \AA}$, where the model fits the data better. These thicknesses also have the lowest uncertainties in both the relative polydispersity (Fig. 7c) and ν (Fig. 7d), and we observe the expected correlation between the thickness and polydispersity in this region: when the thickness increases, the relative polydispersity decreases slightly. However, when the thickness reaches 35 \AA the polydispersity starts to increase slowly, partly because larger thicknesses need a smaller relative polydispersity to give the same absolute polydispersity, and from around 60 \AA and above it becomes increasingly more poorly determined. On the other hand, the effects of a larger polydispersity (the continuation of the q^{-4} slope to lower q values) are suppressed by the observed increase in ν . This feature also explains the complete correlation between the thickness and RPA factor if the polydispersity is large enough: above approximately 0.1 \AA^{-1} there is a q^{-4} slope, and below this q value the excluded volume effect causes the curve to bend, while the fractal structure factor provides the increase in scattering at low q . Therefore, if both the mineral density and polydispersity are large, then SAXS may actually not be sensitive to the thickness at all. And, unfortunately, it is difficult to determine any of the fitting parameters from complementary techniques or theoretical calculations, so we do not know what their values are. Therefore, even though the uncertainties of each parameter are provided during the fitting procedure, they may in reality be considerably larger.

Sample Texture has Similar Effects on the Data as the RPA

An additional possible contributor to uncertainties in the model is the texture of the samples: when we see anisotropy in the 2D scattering in all of our samples, there is almost certainly also directionality in the third direction, which we do not measure. The effect on the plate scattering ($T = 30 \text{ \AA}$) from preferred directionality relative to the incoming beam is demonstrated in Fig. 8, which includes parameter values similar to those found from the measured

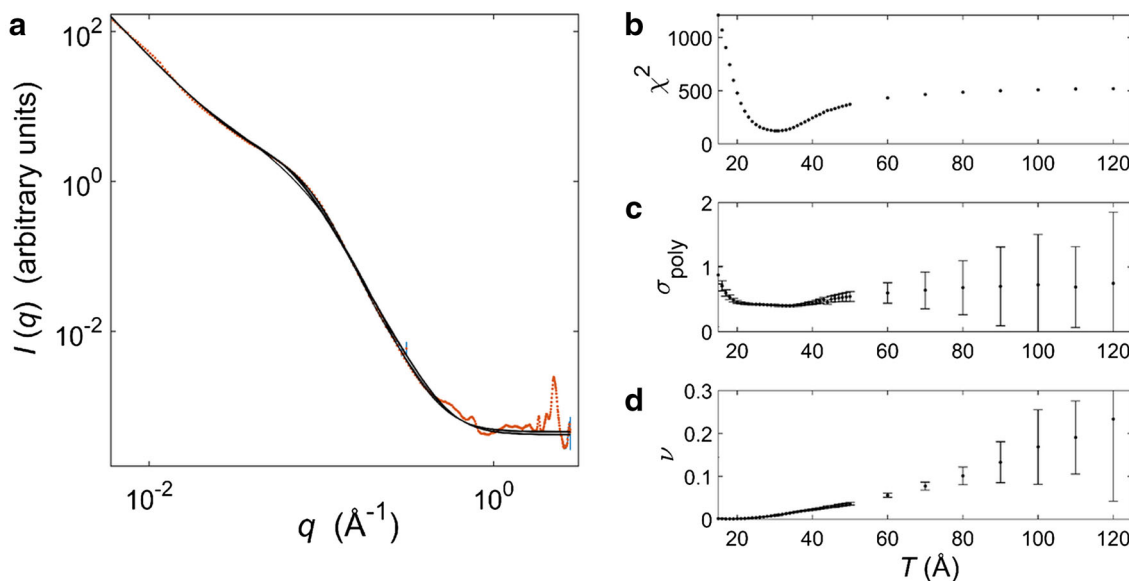


Fig. 7 Fits with thickness fixed from 20 to 200 Å in steps of 10 Å (a), together with the fit quality (b), relative polydispersity (c), and RPA value (d) from the fit procedure as a function of fixed thickness

data. The directionality was described using Gaussian distribution with standard deviations of $\sigma_{\text{Gauss}} = 5^\circ$ (dotted lines), 15° (dash-dotted lines), and 45° (dashed lines) around two angles: with the normal of plate perpendicular to the beam (blue lines) or parallel to the beam (red lines). In order to better identify the effect of texture, the disc was modeled using a finite size with a diameter of 400 Å and a

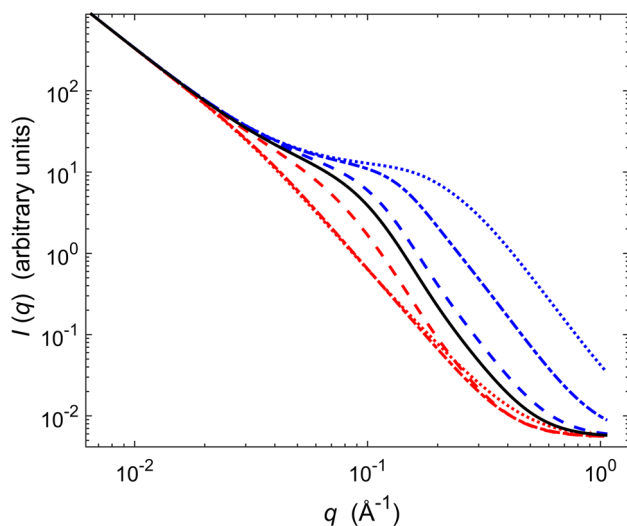


Fig. 8 Demonstration of the influence on the scattering when the plate has a preferred direction described by Gaussian distributions of $\sigma = 5^\circ$ (dotted lines), 15° (dash-dotted lines), and 45° (dashed lines) with the normal of the plate either perpendicular (blue) or parallel (red) to the beam. The full orientational average is shown as a black line (Color figure online)

20 % relative polydispersity in the diameter, which was included to avoid oscillations from this dimension when the plate normal was parallel to the beam. It is clear from Fig. 8 that the data are influenced significantly when the degree of orientation is large (narrow distribution so small σ_{Gauss}). Interestingly, however, all curves, except the two with the highest degree of orientation parallel to the beam (red dotted and dash-dotted lines), can be described perfectly with fully orientationally averaged form factors, where both thickness and polydispersity are fixed at the original values. In other words, it seems that most of the effect on the scattering from texture in the sample influences solely the RPA factor but not the thickness in this model. Since the intensity level at high q is quite different depending on the degree of orientation, however, the value of the Porod constant will differ and thereby also thicknesses extracted with the method that uses this constant.

Alternative Models Have Not Improved the Analysis

Since the model used in this study has some drawbacks in terms of the precision in thickness determination, we have tested other modeling methods. From the atomic structure of the hydroxyapatite unit cell [44], we have constructed models of plates elongated in the c -axis direction and of different thickness and calculated their scattering with both CRY SOL [45] and a method which uses the Debye equation to calculate the scattering as implemented in [46]. As expected, these atomic crystals give too pronounced Bragg peaks, because the actual crystals are expected to have a

significant amount of substitutions and other imperfections [17–19], which would be difficult to include in the modeling. Furthermore, the internal structure does not provide the feature that we assign to polydispersity, and there should also be a significant amorphous layer on the surface [25, 26]. The effect of surface roughness on the data was investigated using a Gaussian smearing of the interfaces [47] in our model instead of polydispersity, but this could not describe the data. To test a structure similar to those proposed in [48] and [12, 13], we implemented a paracrystal model as described in [49] (using the decoupling approximation [50]), where the plates exist in clusters with a finite number of parallel plates (to account for the absence of correlation peak) and a degree of disorder in the plate distances. This model could only fit the data at low q if the fractal structure factor was still included, and then it had too many parameters (two extra compared to the RPA model) to give unambiguous results. Therefore, with our present knowledge of bone nanostructure, we are not able to improve the modeling method. We can only conclude that great attention should be paid when SAXS data from bone samples are analyzed, as many different effects contribute to the scattering pattern.

The Literature Contains Similar Uncertainties of the Thickness

The only parameter that we can compare directly with other studies is the plate thickness, which has been reported in the literature. Atomic force microscopy (AFM) measurements of trabecular bovine bone have reported a plate thickness of 30–100 Å [51], which is similar to our bovine samples from cortical bone. However, other AFM studies of bovine bone show mineral plate thicknesses of 20 Å [52] for young animals and only around 6 Å for mature animals [53]. So for bovine samples alone, the reported span of the plate thickness is 6–100 Å. A TEM study of thin ion-milled section of human cortical bone concludes the average thickness to be around 50 Å [12]. SAXS studies using the Porod region reports average thicknesses of 25–35 Å for different species (not bovine bone) [31], while studies on murine bones using the model described here report thicknesses around 25 Å [34, 54]. One possible explanation for the greater thicknesses sometimes reported in studies using direct measurements of individual plates compared to those obtained from SAXS could be the difficulty of assuring that the plates are truly edge-on in the direct measurements, which may bias the measurements toward larger values. On the other hand, as we have discussed here, SAXS measurements are also subject to different possible uncertainties. The variation in the reported thicknesses emphasizes the need for more precise measurements

or more systematic comparisons between different animals and/or tissues with the same methods.

Conclusion

Freshly cut bone samples at three different directions and from different species presented in this study display a remarkable similarity of their azimuthally averaged scattering data. The small-angle scattering is similar in all three directions, while the wide-angle scattering confirms the plates to have the predominant direction of its c -axis parallel to long axis of the bone. The absence of a correlation peak in the data establishes that the mineral plates are not arranged in extended stacks with a characteristic separation and long-range order.

We have obtained the crystal plate thicknesses of the samples using what we believe is the best available model. Concentration effects due to high mineral volume fraction and a large degree of polydispersity of the plates cause the analysis to be extremely difficult due to correlation of model parameters. Therefore, one should be exceedingly careful when SAXS is used to study mineral plates in bone, as the uncertainties can be larger than one initially may think. All things considered, our data indicate that the thickness of the plates in the samples presented here is 20–40 Å for most samples, while the bovine samples apparently have thicker plates at around 40–60 Å.

Acknowledgments Funding from the Swedish Foundation for Strategic Research and the European Commission (FRACQUAL-293434) is gratefully acknowledged.

Compliance with Ethical Standards

Conflict of Interest None of the authors have any conflict of interest.

Human and Animal Rights and Informed Consent All applicable international, national, and/or institutional guidelines for the care and use of animals were followed.

References

1. Reznikov N, Shahar R, Weiner S (2014) Bone hierarchical structure in three dimensions. *Acta Biomater* 10(9):3815–3826. doi:[10.1016/j.actbio.2014.05.024](https://doi.org/10.1016/j.actbio.2014.05.024)
2. Fratzl P, Gupta HS, Paschalis EP, Roschger P (2004) Structure and mechanical quality of the collagen-mineral nano-composite in bone. *J Mater Chem* 14(14):2115–2123. doi:[10.1039/b402005g](https://doi.org/10.1039/b402005g)
3. Stock SR (2015) The mineral-collagen interface in bone. *Calcif Tissue Int*. doi:[10.1007/s00223-015-9984-6](https://doi.org/10.1007/s00223-015-9984-6)
4. Hodge AJ, Petruska JA (1963) Recent studies with the electron microscope on ordered aggregates of the tropocollagen molecule. In: Ramachandran GN (ed) *Aspects of protein structure*. Academic press, London and New York, pp 289–300

5. Landis WJ, Jacquet R (2013) Association of calcium and phosphate ions with collagen in the mineralization of vertebrate tissues. *Calcif Tissue Int* 93(4):329–337. doi:[10.1007/s00223-013-9725-7](https://doi.org/10.1007/s00223-013-9725-7)
6. Weiner S, Arad T, Traub W (1991) Crystal organization in rat bone lamellae. *FEBS Lett* 285(1):49–54. doi:[10.1016/0014-5793\(91\)80722-F](https://doi.org/10.1016/0014-5793(91)80722-F)
7. Landis WJ, Hodgens KJ, Song MJ, Arena J, Kiyonaga S, Marko M, Owen C, McEwen BF (1996) Mineralization of collagen may occur on fibril surfaces: evidence from conventional and high-voltage electron microscopy and three-dimensional imaging. *J Struct Biol* 117(1):24–35. doi:[10.1006/jbsi.1996.0066](https://doi.org/10.1006/jbsi.1996.0066)
8. Olszta MJ, Cheng X, Jee SS, Kumar R, Kim Y-Y, Kaufman MJ, Douglas EP, Gower LB (2007) Bone structure and formation: a new perspective. *Mater Sci Eng* 58(3–5):77–116. doi:[10.1016/j.mser.2007.05.001](https://doi.org/10.1016/j.mser.2007.05.001)
9. Chen PY, Toroian D, Price PA, McKittrick J (2011) Minerals form a continuum phase in mature cancellous bone. *Calcif Tissue Int* 88(5):351–361. doi:[10.1007/s00223-011-9462-8](https://doi.org/10.1007/s00223-011-9462-8)
10. Weiner S, Price PA (1986) Disaggregation of bone into crystals. *Calcif Tissue Int* 39(6):365–375. doi:[10.1007/Bf02555173](https://doi.org/10.1007/Bf02555173)
11. McNally E, Nan F, Botton GA, Schwarcz HP (2013) Scanning transmission electron microscopic tomography of cortical bone using Z-contrast imaging. *Micron* 49:46–53. doi:[10.1016/j.micron.2013.03.002](https://doi.org/10.1016/j.micron.2013.03.002)
12. McNally EA, Schwarcz HP, Botton GA, Arsenault AL (2012) A model for the ultrastructure of bone based on electron microscopy of ion-milled sections. *PLoS One*. doi:[10.1371/journal.pone.0029258](https://doi.org/10.1371/journal.pone.0029258)
13. Schwarcz HP, McNally EA, Botton GA (2014) Dark-field transmission electron microscopy of cortical bone reveals details of extrafibrillar crystals. *J Struct Biol* 188(3):240–248. doi:[10.1016/j.jsb.2014.10.005](https://doi.org/10.1016/j.jsb.2014.10.005)
14. Fujisawa R, Kuboki Y (1991) Preferential adsorption of dentin and bone acidic proteins on the (100) face of hydroxyapatite crystals. *Biochim Biophys Acta* 1:56–60
15. Wang ZQ, Xu ZJ, Zhao WL, Sahai N (2015) A potential mechanism for amino acid-controlled crystal growth of hydroxyapatite. *J Mater Chem B* 3(47):9157–9167. doi:[10.1039/c5tb01036e](https://doi.org/10.1039/c5tb01036e)
16. Hu YY, Rawal A, Schmidt-Rohr K (2010) Strongly bound citrate stabilizes the apatite nanocrystals in bone. *Proc Natl Acad Sci USA* 107(52):22425–22429. doi:[10.1073/pnas.1009219107](https://doi.org/10.1073/pnas.1009219107)
17. Handschin RG, Stern WB (1995) X-ray diffraction studies on the lattice perfection of human bone apatite (Crista Iliaca). *Bone*. doi:[10.1016/S8756-3282\(95\)80385-8](https://doi.org/10.1016/S8756-3282(95)80385-8)
18. Handschin RG, Stern WB (1992) Crystallographic lattice refinement of human bone. *Calcif Tissue Int* 51(2):111–120. doi:[10.1007/Bf00298498](https://doi.org/10.1007/Bf00298498)
19. Trebacz H, Pikus S (2003) A study of mineral phase in immobilized rat femur: structure refinements by Rietveld analysis. *J Bone Miner Metab* 21(2):80–85. doi:[10.1007/s007740300013](https://doi.org/10.1007/s007740300013)
20. Selvig KA (1970) Periodic lattice images of hydroxyapatite crystals in human bone and dental hard tissues. *Calcif Tiss Res* 6(3):227–238. doi:[10.1007/Bf02196203](https://doi.org/10.1007/Bf02196203)
21. Schmidt WI (1936) Über die Orientierung der Kristallite im Zahnschmel. *Naturwissenschaften* 24(23):361. doi:[10.1007/BF01473678](https://doi.org/10.1007/BF01473678)
22. Tadano S, Giri B (2011) X-ray diffraction as a promising tool to characterize bone nanocomposites. *Sci Technol Adv Mater*. doi:[10.1088/1468-6996/12/6/064708](https://doi.org/10.1088/1468-6996/12/6/064708)
23. Meneghini C, Dalconi MC, Nuzzo S, Mobilio S, Wenk RH (2003) Rietveld refinement on X-ray diffraction patterns of bioapatite in human fetal bones. *Biophys J* 84(3):2021–2029. doi:[10.1016/S0006-3495\(03\)75010-3](https://doi.org/10.1016/S0006-3495(03)75010-3)
24. Smith CB, Smith DA (1978) Structural role of bone apatite in human femoral compacta. *Acta Orthop Scand* 49(5):440–444. doi:[10.3109/17453677808993259](https://doi.org/10.3109/17453677808993259)
25. Wang Y, Von Euw S, Fernandes FM, Cassaignon S, Selmane M, Laurent G, Pehau-Arnaudet G, Coelho C, Bonhomme-Courry L, Giraud-Guille M-M, Babonneau F, Azaïs T, Nassif N (2013) Water-mediated structuring of bone apatite. *Nat Mater* 12(12):1144–1153. doi:[10.1038/nmat3787](https://doi.org/10.1038/nmat3787)
26. Jager C, Welzel T, Meyer-Zaika W, Epple M (2006) A solid-state NMR investigation of the structure of nanocrystalline hydroxyapatite. *Magn Reson Chem* 44(6):573–580. doi:[10.1002/Mrc.1774](https://doi.org/10.1002/Mrc.1774)
27. Wilson EE, Awonusi A, Morris MD, Kohn DH, Tecklenburg MMJ, Beck LW (2005) Highly ordered interstitial water observed in bone by nuclear magnetic resonance. *J Bone Miner Res* 20(4):625–634. doi:[10.1359/JBMR.041217](https://doi.org/10.1359/JBMR.041217)
28. Weiner S, Traub W (1992) Bone-structure—from Angstroms to Microns. *Faseb Journal* 6(3):879–885
29. Boskey A (2003) Bone mineral crystal size. *Osteoporos Int* 14:S16–S20. doi:[10.1007/s00198-003-1468-2](https://doi.org/10.1007/s00198-003-1468-2)
30. Fratzl P, Groschner M, Vogl G, Plenk H, Eschberger J, Fratzlzelman N, Koller K, Klaushofer K (1992) Mineral crystals in calcified tissues—a comparative-study by saxs. *J Bone Miner Res* 7(3):329–334
31. Fratzl P, Schreiber S, Klaushofer K (1996) Bone mineralization as studied by small-angle X-ray scattering. *Connect Tissue Res* 35(1–4):9–16
32. Fratzl P, Fratzlzelman N, Klaushofer K, Vogl G, Koller K (1991) Nucleation and growth of mineral crystals in bone studied by small-angle X-ray-scattering. *Calcif Tissue Int* 48(6):407–413. doi:[10.1007/Bf02556454](https://doi.org/10.1007/Bf02556454)
33. Hiller JC, Wess TJ (2006) The use of small-angle X-ray scattering to study archaeological and experimentally altered bone. *J Archaeol Sci* 33(4):560–572. doi:[10.1016/j.jas.2005.09.012](https://doi.org/10.1016/j.jas.2005.09.012)
34. Bunger MH, Oxlund H, Hansen TK, Sorensen S, Bibby BM, Thomsen JS, Langdahl BL, Besenbacher F, Pedersen JS, Birkedal H (2010) Strontium and bone nanostructure in normal and ovariectomized rats investigated by scanning small-angle X-ray scattering. *Calcif Tissue Int* 86(4):294–306. doi:[10.1007/s00223-010-9341-8](https://doi.org/10.1007/s00223-010-9341-8)
35. Fratzl P, Gupta HS, Paris O, Valenta A, Roschger P, Klaushofer K (2005) Diffracting “stacks of cards”—some thoughts about small-angle scattering from bone. In: Kremer F, Richtering W (eds) *Scattering methods and the properties of polymer materials*, vol 130., Progress in colloid and polymer scienceSpringer, Berlin, pp 33–39
36. Acerbo AS, Kwaczala AT, Yang L, Judex S, Miller LM (2014) Alterations in collagen and mineral nanostructure observed in osteoporosis and pharmaceutical treatments using simultaneous small- and wide-angle X-ray scattering. *Calcif Tissue Int* 95(5):446–456. doi:[10.1007/s00223-014-9913-0](https://doi.org/10.1007/s00223-014-9913-0)
37. Georgiadis M, Guizar-Sicairos M, Zwahlen A, Trussel AJ, Bunk O, Muller R, Schneider P (2015) 3D scanning SAXS: a novel method for the assessment of bone ultrastructure orientation. *Bone* 71:42–52. doi:[10.1016/j.bone.2014.10.002](https://doi.org/10.1016/j.bone.2014.10.002)
38. Burger C, Zhou HW, Wang H, Sics I, Hsiao BS, Chu B, Graham L, Glimcher MJ (2008) Lateral packing of mineral crystals in bone collagen fibrils. *Biophys J* 95(4):1985–1992. doi:[10.1529/biophysj.107.128355](https://doi.org/10.1529/biophysj.107.128355)
39. Lindner P, Zemb T (2002) *Neutrons, X-rays, and light: scattering methods applied to soft condensed matter*, 1st edn., North-Holland delta series, Elsevier, Amsterdam, Boston
40. Shimada T, Doi M, Okano K (1988) Concentration fluctuation of stiff polymers. 1. Static structure factor. *J Chem Phys* 88(4):2815–2821. doi:[10.1063/1.454016](https://doi.org/10.1063/1.454016)
41. Teixeira J (1988) Small-angle scattering by fractal systems. *J Appl Crystallogr* 21:781–785. doi:[10.1107/s0021889888000263](https://doi.org/10.1107/s0021889888000263)
42. Wagermaier W, Gupta HS, Gourrier A, Burghammer M, Roschger P, Fratzl P (2006) Spiral twisting of fiber orientation inside bone lamellae. *Biointerphases* 1(1):1–5. doi:[10.1116/1.2178386](https://doi.org/10.1116/1.2178386)

43. Schweizer KS, Curro JG (1994) Prism theory of the structure, thermodynamics, and phase-transitions of polymer liquids and alloys. *Adv Polym Sci* 116:319–377. doi:[10.1007/Bfb0080203](https://doi.org/10.1007/Bfb0080203)
44. Hughes JM, Cameron M, Crowley KD (1989) Structural variations in natural F, OH, and Cl apatites. *Am Miner* 74(7–8):870–876
45. Svergun D, Barberato C, Koch MHJ (1995) CRY SOL—a program to evaluate X-ray solution scattering of biological macromolecules from atomic coordinates. *J Appl Crystallogr* 28:768–773
46. Døvling Kaspersen J, Moestrup Jessen C, Stougaard Vad B, Skipper Sørensen E, Kleiner Andersen K, Glasius M, Pinto Oliveira CL, Otzen DE, Pedersen JS (2014) Low-Resolution structures of OmpA-DDM protein-detergent complexes. *ChemBioChem* 15(14):2113–2124. doi:[10.1002/cbic.201402162](https://doi.org/10.1002/cbic.201402162)
47. Pedersen JS (1999) Structural studies by small-angle scattering and specular reflectivity. Riso National Lab, Roskilde
48. Traub W, Arad T, Weiner S (1989) 3-Dimensional ordered distribution of crystals in Turkey tendon collagen-fibers. *Proc Natl Acad Sci USA* 86(24):9822–9826. doi:[10.1073/pnas.86.24.9822](https://doi.org/10.1073/pnas.86.24.9822)
49. Pedersen JS, Vyskocil P, Schonfeld B, Kostorz G (1997) Small-angle neutron scattering of precipitates in Ni-rich Ni-Ti alloys. II. Methods for analyzing anisotropic scattering data. *J Appl Crystallogr* 30:975–984
50. Kotlarchyk M, Chen SH (1983) Analysis of small-angle neutron-scattering spectra from polydisperse interacting colloids. *J Chem Phys* 79(5):2461–2469
51. Hassenkam T, Fantner GE, Cutroni JA, Weaver JC, Morse DE, Hansma PK (2004) High-resolution AFM imaging of intact and fractured trabecular bone. *Bone* 35(1):4–10. doi:[10.1016/j.bone.2004.02.024](https://doi.org/10.1016/j.bone.2004.02.024)
52. Tong W, Glimcher MJ, Katz JL, Kuhn L, Eppell SJ (2003) Size and shape of mineralites in young bovine bone measured by atomic force microscopy. *Calcif Tissue Int* 72(5):592–598. doi:[10.1007/s00223-002-1077-7](https://doi.org/10.1007/s00223-002-1077-7)
53. Eppell SJ, Tong WD, Katz JL, Kuhn L, Glimcher MJ (2001) Shape and size of isolated bone mineralites measured using atomic force microscopy. *J Orthop Res* 19(6):1027–1034. doi:[10.1016/S0736-0266\(01\)00034-1](https://doi.org/10.1016/S0736-0266(01)00034-1)
54. Turunen MJ, Lages S, Labrador A, Olsson U, Tagil M, Jurvelin JS, Isaksson H (2014) Evaluation of composition and mineral structure of callus tissue in rat femoral fracture. *J Biomed Opt*. doi:[10.1117/1.Jbo.19.2.025003](https://doi.org/10.1117/1.Jbo.19.2.025003)